

# Modeling the SpaceX Falcon-9 Booster's Triple Sonic Boom Using Multiple Models and Conditions

Mark C. Anderson\* and Kent L. Gee<sup>†</sup> *Brigham Young University, Provo, UT 84602* 

In the age of commercial spaceflight, many organizations are designing rockets for reuse. Most designs employ some form of propulsive landing either on land or at sea. The foremost among these organizations is Space Exploration Technologies Corporation (SpaceX) with their Falcon-9 rocket. As such rockets return, they produce audible sonic booms over the surrounding areas. The Falcon-9 booster's sonic boom signature is unique, consisting of three primary shocks instead of the two associated with traditional N-waves. This provides an opportunity to study sonic boom formation from a unique geometry and to see whether the triple boom can be physically explained. This paper considers F-function and computational fluid dynamics methods to model the booster's sonic boom under conditions ranging from Mach 1.5 to 2.5. Results support the conclusion of Anderson and Gee (2025) [JASA Express Lett. 5, 023601 (2025)] that the central shock is the result of a rearward-migrating rarefaction wave produced by the lower portions of the booster merging with a forward-migrating compression wave produced by the grid fins. Although it is clear that both the grid fins and the lower portions of the booster contribute to the central shock, the different models disagree on their relative importance in producing the final shock.

### I. Introduction

As the global launch cadence increases, sonic booms from rockets are becoming increasingly common. Launch vehicles produce sonic booms on ascent and descent [1–4], regardless of whether the descent is controlled or not. Typically, these sonic booms occur over the ocean and seldom impinge on land. However, when a rocket is intentionally flown back to land for reuse, it produces an audible sonic boom on land. These sonic booms, sometimes referred to as "flyback booms" [5, 6], can persist to distances at least as far as 25 km from the landing location [5] and represent a phenomenon that will become more common as different organizations pursue rocket reusability.

Having landed their Falcon-9 rocket hundreds of times, Space Exploration Technologies Corporation (SpaceX) is the dominant organization producing reusable rockets [7]. A typical flight profile proceeds as follows [8]: the two-stage Falcon-9 rocket lifts off using the thrust of nine booster-stage engines. The booster lifts the upper stage and payload high into the atmosphere before separating. While the upper stage and payload continue to orbit, the booster stage either continues to coast downrange to a barge landing or reverses orientation and reignites its engines to travel back to the launch site. After a coast phase lasting a few minutes, while still around 50 km or higher in altitude, the booster ignites 1–3 engines for the "entry burn", which slows the booster before entering the thicker atmosphere at lower altitudes. Finally, after another brief coast phase, the booster ignites 1–3 engines one more time shortly before extending its landing legs and touching down softly on the landing pad.

While NASA and other agencies have studied the effects of traditional aircraft sonic booms on structures and human response for several decades [9], little research has been performed on these rocket flyback sonic booms. Aside from initial data collection and analysis efforts [5, 10–12], another important step is to attempt physics-based modeling of the unique features of these sonic booms. For example, while most sonic booms tend toward N-wave shapes (with two shocks) [9], Falcon 9 flyback sonic booms tend toward a triple-boom signature with three primary shocks [5]. The three shocks show little to no sign of evolution toward an N-wave, and the total sonic boom duration remains nearly constant at all distances from the landing location [5, 12]. Although sonic boom signatures with three primary shocks have been measured before (see several examples in Maglieri et al. [9]), ensuring that the reasons for the Falcon 9 booster's triple sonic boom are understood can provide insight into future flyback boom predictions. For example, it is already known

<sup>\*</sup>PhD Candidate, Brigham Young University Department of Physics and Astronomy, ESC-N283 N Campus Drive Provo, UT 84602, Student Member.

<sup>†</sup>Professor, Brigham Young University Department of Physics and Astronomy, ESC-N283 N Campus Drive Provo, UT 84602, Fellow.

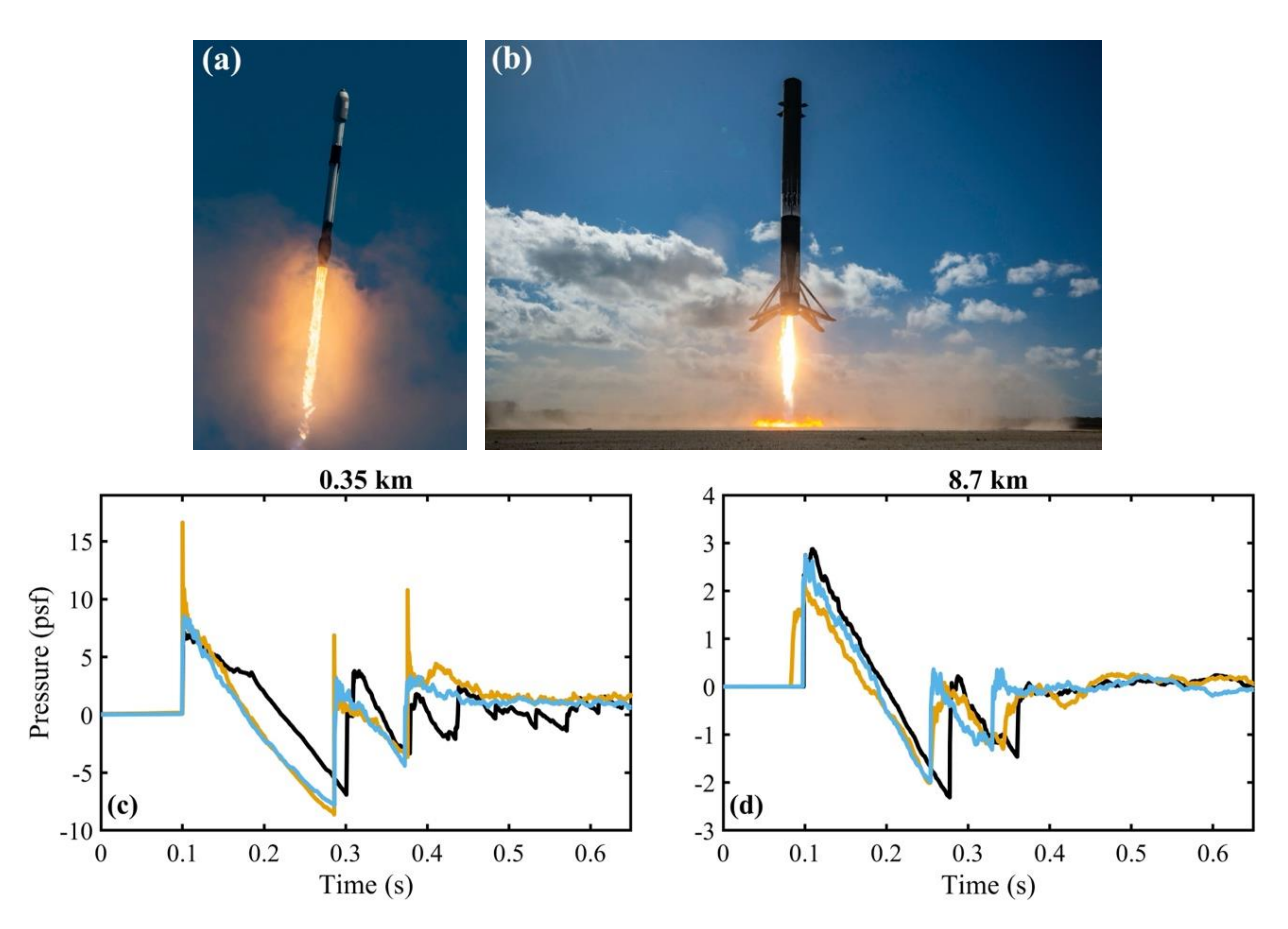


Fig. 1 (a) A full Falcon-9 rocket shortly after liftoff. (b) A Falcon-9 booster moments before a successful landing. (c) Sonic boom waveforms measured 0.35 km away from the landing pad during three different missions. (d) Sonic boom waveforms measured 8.7 km away from the landing pad during the same three missions. [This entire figure is reproduced from Ref. [6] without changes (CC BY-NC 4.0 DEED License). Credit for photographs (a) and (b): SpaceX (CC BY-NC 2.0 DEED License. No changes made).]

that the SpaceX Starship Super Heavy booster also produces a triple sonic boom [13]. Understanding the physics can help determine whether this is a universal feature expected from all rocket flyback events.

Recent work by Anderson and Gee [6] indicates that the triple-boom signature is a direct consequence of the booster's geometry. Using Whitham's F-function paired with numerical propagation via the Burgers equation, they show that the center shock can be explained as the product of a forward-traveling shock wave produced by the grid fins and a backward-traveling shock produced by rarefaction waves near the base of the booster, including the folded landing legs. The resultant shock is more balanced and does not migrate as rapidly to merge with either the front or rear shocks. The calculations were carried out using both a plain cylinder of equal proportions to the booster and a cylinder with protrusions representing the folded landing legs and the grid fins. While the plain cylindrical geometry produced a signature that ultimately evolved into an N-wave, the signature from the more-realistic geometry became a triple boom in the far field. Simple computational fluid dynamics (CFD) simulations and photographic evidence shown in Ref. [6] support the results from the Whitham-Burgers approach.

The goal of this paper is to expand on the work of Ref. [6] and this paper proceeds as follows. In Section II, the near-field pressure signatures are estimated using F-function and CFD approaches. The propagation modeling is discussed in Section III. In Section IV, the near-field signatures are propagated to the far field. Section V then contains a summary of the conclusions found in this paper. Two appendices are also included that contain more CFD results and a validation case for the propagation code.

# **II. Determining Near-field Pressures**

The Falcon-9 booster shows little similarity to traditional aircraft. A schematic is provided in Fig. 2, indicating some unique geometrical aspects of this vehicle. As the vehicle descends, its engine section faces the oncoming flow. The grid fins near the top of the booster also represent a unique flow feature not seen on traditional aircraft. These grid fins are used to control the booster aerodynamically on descent and the flow around and through them is complicated [14].

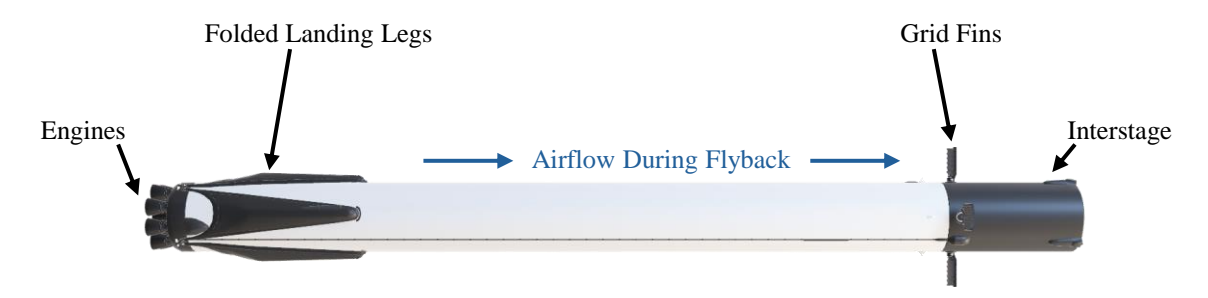


Fig. 2 A Falcon-9 booster. Important parts of its geometry, along with the airflow direction, are indicated. This figure is reproduced from Ref. [6] without changes (CC BY-NC 4.0 DEED License). The original 3D model comes from [15] (CC BY 4.0 DEED License. Changes made.).

In this section, approximate near-field pressure distributions are obtained via the Whitham F-function [9, 16] and CFD. Each has trade-offs. The Whitham F-function assumes first order flow details, which is unlikely to be strictly accurate for such a blunt geometry. Meanwhile, due to the prohibitively high cost of three-dimensional simulations under the resources allotted to the current analysis, the CFD models are two-dimensional and do not capture the full three-dimensional flow field. Nevertheless, it is assumed that these methods all produce near-field pressure distributions that are sufficient to permit a study of the overall waveform shape, though the shock amplitudes and exact positions are not expected to be perfectly accurate. It is strongly recommended that future wind-tunnel tests and three-dimensional CFD simulations be used to determine the full pressure distribution around the booster. Similar tests have been performed before [14, 17, 18], but the focus was on vehicle loads and not on sonic boom prediction.

## A. Whitham F-function

The first-order theory [9, 16] for the flow field around a supersonic projectile estimates the pressure field according to

$$\delta p = \frac{p_a \gamma M_{\infty}^2}{(2\beta r_0)^{1/2}} F(x) \tag{1}$$

where  $\delta p$  is the pressure change from ambient,  $p_a$  is the ambient pressure,  $\gamma$  is the ratio of specific heats,  $M_{\infty}$  is the free-stream Mach number,  $\beta$  is the quantity  $\sqrt{M_{\infty}^2 - 1}$ ,  $r_0$  is the distance from the vehicle, and x is the lengthwise location along the geometry. The quantity F(x) is known as the "F-function", and it represents the specific geometry being modeled. Strictly speaking, the coordinate x should be replaced with  $\chi = x - \beta r_0$ , but it is assumed that  $\chi \approx x$  for the current analysis because blunt objects tend to produce shocks that do not initially propagate along the far-field Mach lines [19].

#### 1. Modifications to the Booster's Blunt Geometry

Although F-function methods were originally developed for use with slender bodies, Carlson and Mack [19] noted that the slender-body theory still tends to work well when applied to blunt geometries for the purpose of sonic boom prediction. To further improve predictions, methods proposed by Gottlieb and Ritzel [20] are applied in this paper to improve shock placement around the blunt geometries.

The Falcon-9 booster has three primary blunt features: the bottom where the engines are located, the grid fins jutting out from the side of the booster, and the top of the booster where the geometry abruptly terminates. As for any supersonic blunt body, a detached bow shock is expected at the base of the booster. To account for the standoff distance between the shock and the body of the booster, an artificial body extension is added to the bottom, ensuring that the shock occurs at the proper location. This extension can be represented by a cubic polynomial

$$g(x) = ax^3 + bx^2 + cx + d (2)$$

subject to boundary conditions. At the tip of the extension, the extension radius  $(R_0)$  goes to zero and the slope goes to

$$R_0' = \beta \left( \frac{3(\gamma + 1)^2}{4M_\infty^2} \right)^{-1/4}.$$
 (3)

However, this produces a new tip that still exceeded the bluntness criteria used by Gottlieb and Ritzel [20]. Therefore, a later definition in [20], designed for blunt features along the body, was used and found to produce a tip that was closer to meeting the bluntness criteria. This definition is

$$R_0' = \frac{2}{\gamma + 1} \frac{\beta^2}{M_{\infty}^2}.\tag{4}$$

This definition of  $R'_0$  was used to produce new effective tips for the blunt geometries. Additionally, the extension must match the radius  $(R_1)$  and slope  $(R'_1)$  of the booster body where it joins the booster. The final constraint is that the extension must be of length

$$\Delta x = \frac{3R_1}{2R_0' + R_1'} \tag{5}$$

which is then converted into a coordinate for the tip of the extension  $(x_0)$ . Lastly, the extension base should be located at the same location as the bottom of the booster  $(x_1)$ . With all of these conditions in place, the cubic polynomial coefficients representing the extension can be solved for via

$$\begin{bmatrix} x_0^3 & x_0^2 & x_0 & 1\\ 3x_0^2 & 2x_0 & 1 & 0\\ x_1^3 & x_1^2 & x_1 & 1\\ 3x_1^2 & 2x_1 & 1 & 0 \end{bmatrix} \begin{bmatrix} a\\b\\c\\d \end{bmatrix} = \begin{bmatrix} R_0\\R'_0\\R_1\\R'_1 \end{bmatrix}.$$
 (6)

For blunt features that occur after the front of the geometry (like the grid fins on the booster), the process is largely the same, with a few small changes. The required slope at the point where the extension touches the body is calculated via Eq. 4 and the standoff distance is

$$\Delta x = \frac{3(R_1 - R_0)}{2R_0' + R_1'} \tag{7}$$

which is then converted into the coordinate  $x_0$ . The grid fins in this paper are modeled exactly as in Ref. [6], treating the grid fins as smaller protuberances to allow airflow past them while still producing a shock.

For blunt features that face away from the flow, like the top of the booster, a different type of extension is applied to the body. This extension accounts for the flow after the body and the subsequent turbulent wake. The first portion of the extended geometry is a conical shape that gets smaller with distance behind the top of the booster. The initial radius of the cone must match the top of the booster and the length of the cone is

$$L = 2R(1.83 - 0.186M_{\infty}) \tag{8}$$

where *R* is the radius of the booster. The conical geometry does not come to a point at this distance, but rather reaches a radius of

$$R_w = R(0.950 - 0.150M_{\infty}) \tag{9}$$

were  $R_w$  is the radius of the turbulent wake. After this point, the turbulent wake in this paper is modeled simply as a constant cylindrical body extending behind the booster.

The modified geometries are shown in Fig. 3 for (a) a plain cylinder that represents a Falcon-9 booster without landing legs or grid fins and (b) a cylindrical body that contains protrusions representing the booster's folded landing legs and extended grid fins.

#### 2. Calculating the F-function

The Whitham F-function F(x) is defined as [9, 16]

$$F(x) = \frac{1}{2\pi} \int_0^x \frac{A''(\bar{x})}{\sqrt{x - \bar{x}}} d\bar{x}$$
 (10)

where A''(x) is the second derivative of the cross-sectional area as a function of distance x along the body. Strictly speaking, the cross-section should be taken along slices at the Mach angle, but Carlson and Mack [19] suggest that for blunt bodies it may be more appropriate to use slices that are normal to the geometry as the initial shocks around a blunt body tend not to immediately propagate away at the far-field Mach angle. In this paper, A''(x) is calculated normal to the geometry. The final F-functions are shown in Fig. 3.

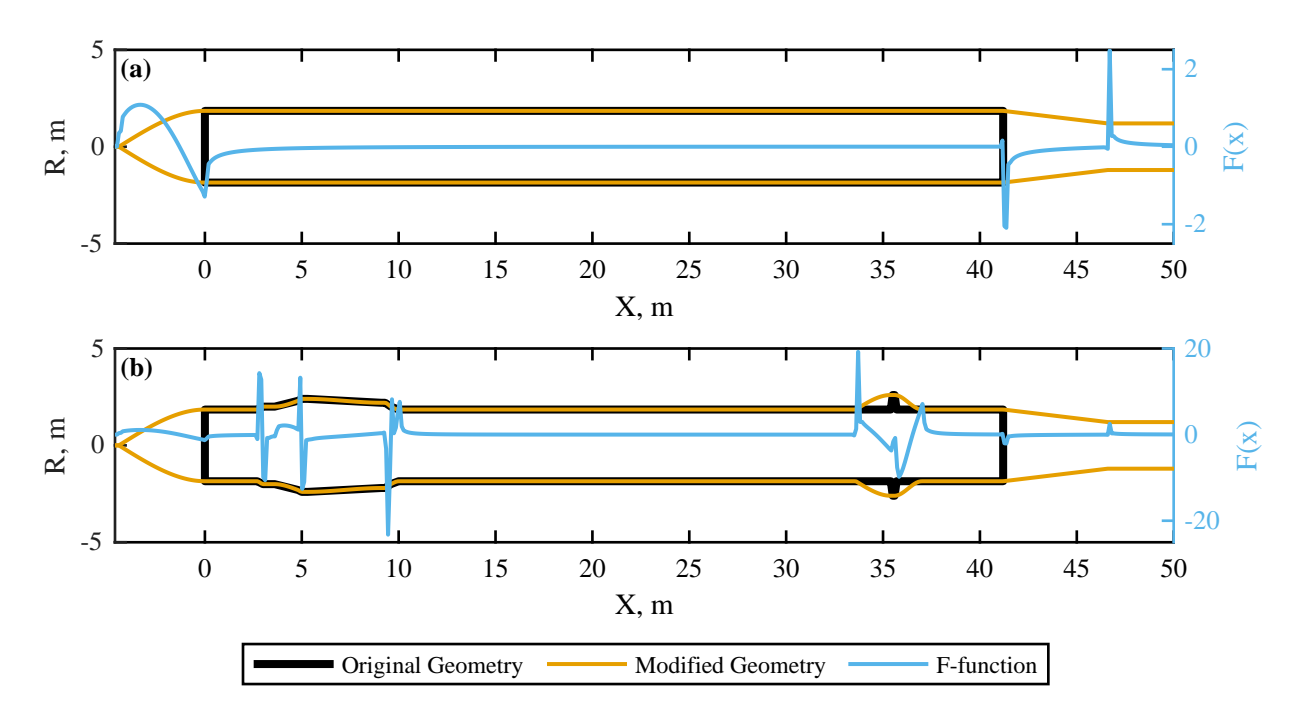


Fig. 3 The Falcon-9 booster modeled in two levels of detail. (a) The booster modeled as a simple cylinder. (b) The booster modeled as a cylinder with protuberances representing the folded landing legs and the grid fins. The geometry modifications were calculated at Mach 2.0.

The F-functions in Fig. 3 are then converted into pressures via Eq. 1 (with  $r_0 = 41.2$  m) and the results are shown in Fig. 4. Immediately, a problem becomes obvious in the predicted pressure magnitudes. The negative pressure magnitudes drop below 1 atmosphere, a phenomenon that is not possible in real fluid flow at an ambient pressure of 1 atm. Additionally, some positive pressure values appear improbably large. This was also noted in Ref. [6], where it was observed that shock formation and decay rapidly decreased these pressure amplitudes to more-realistic values within the first few meters of propagation. Thus, although further investigation into the physicality of F-function results for descending rocket boosters needs to be performed, it is assumed in this paper that the propagated results will be good enough for determining the overall waveform shape after propagation. However, the final pressure amplitudes are unlikely to be fully accurate.

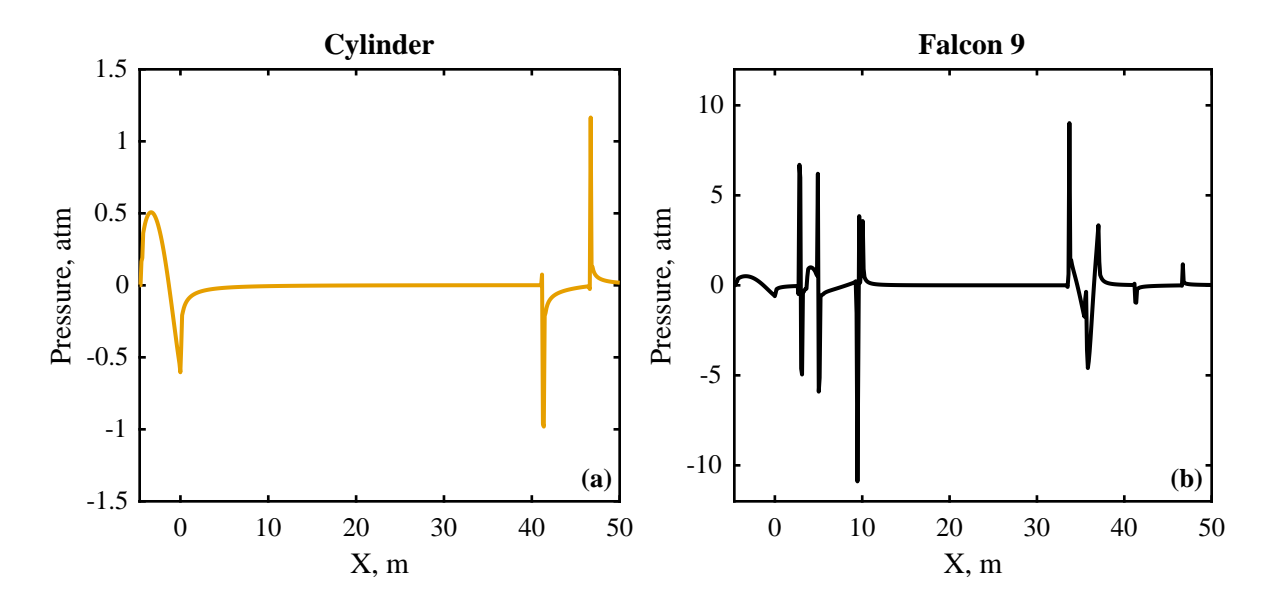


Fig. 4 The calculated pressures around the (a) Cylinder and (b) Falcon-9 geometries at Mach 2.0. and a linearly-propagated distance of  $r_0 = 41.2$  m.

## B. Computational Fluid Dynamics (CFD)

Another method to obtain the pressures in the flow field surrounding a supersonic vehicle is CFD. For the results in this paper, two-dimensional unstructured meshes for both the Cylinder and Falcon-9 geometries were produced in GMSH [21] and the simulations were run in OpenFOAM 11 [22]. The simulations were run with the *shockFluid* solver for compressible flows. Assuming symmetry, the flow was only computed on one side of the geometries, with a *symmetryPlane* boundary condition on the bottom. Further details for each boundary condition are given in Table 1. For these simulations, a  $k-\omega$  Shear Stress Transport (SST) turbulence model was used. The initial estimates at the boundaries were solved via the following equations [23, 24]:

$$k = \frac{3}{2}(UI)^2 \tag{11}$$

$$\omega = \frac{\sqrt{k}}{C_{\mu}^{1/4} \ell} \tag{12}$$

$$v_t = \frac{k}{\omega} \tag{13}$$

where k is the turbulent kinetic energy, U is the freestream velocity, I is the turbulence intensity (taken to be 0.05 throughout this paper),  $\omega$  is the specific turbulent dissipation rate,  $C_{\mu} = 0.09$ ,  $\ell$  is the turbulent length scale (taken to be 0.25 m throughout this paper), and  $v_t$  is related to the turbulent viscosity. Calculated values are tabulated in Table 2 alongside other flow parameters.

There are two main benefits to using CFD to obtain near-field pressures rather than relying on F-function methods. First, blunt portions of the geometry can be modeled directly without needing to make assumptions about shock location and strength. Second, the grid fins can be more appropriately modeled. Meshes for the Cylinder and Falcon-9 geometries are shown in Fig. 5, including a close view of the grid fins. The fins are modeled using seven diamond-shaped elements to approximate the number of struts used in the physical grid fins. This approximation allows for a better simulation of the flow through the fins and the shock structure produced by the fins. This is an improvement over what was done in Ref. [6], where the same geometry used for F-function analysis was used in the CFD analysis.

Simulations were run at Mach 1.5, 2.0, and 2.5, and zoomed-in pressure fields shown in Fig. 6. In the near field, the Cylinder produces a triple sonic boom consisting of the bow shock followed by a rarefaction wave which steepens into a shock and then ending with the wake shock. This same overall structure is observed at all three Mach numbers. In constrast, the Falcon-9 geometry produces many more near-field shocks at each Mach number, and those shocks can

Table 1 Boundary conditions used in the CFD simulations. The inlet was located on the left boundary and the outlet on the top and right boundaries.

	inlet	outlet	vehicle	bottom	
alphat	calculated	waveTransmissive	compressible::alphatWallFunction	symmetryPlane	
k	fixedValue	waveTransmissive	kqrWallFunction	symmetryPlane	
nut	calculated	waveTransmissive	nutkWallFunction	symmetryPlane	
omega	fixedValue	waveTransmissive	omegaWallFunction	symmetryPlane	
p	fixedValue	waveTransmissive	zeroGradient	symmetryPlane	
T	fixedValue	waveTransmissive	zeroGradient	symmetryPlane	
U	fixedValue	waveTransmissive	noSlip	symmetryPlane	

Table 2 Flow properties for each of the simulations.

	alphat	k	nut	omega	р	T	U
	(kg/m s)	$(\mathbf{m}^2/\mathbf{s}^2)$	$(\mathbf{m}^2/\mathbf{s})$	(1/s)	$(kg/m s^2)$	<b>(K)</b>	( <b>m/s</b> )
M = 1.5	0	975	4.27	228	1e5	300	(510, 0, 0)
M = 2.0	0	1734	5.70	304	1e5	300	(680, 0, 0)
M = 2.5	0	2709	7.12	380	1e5	300	(850, 0, 0)

be seen beginning to coalesce with distance from the booster. While these are zoomed-in results, the full calculated domains can be seen in Appendix A.

Finally, the CFD results can be used to extract pressures along lines parallel to the geometries. To be thorough, pressures were extracted along three different lines corresponding to different distances from the geometries (10, 20, and 41.2 m). The freestream pressure was then subtracted and the amplitude effects of cylindrical spreading were then approximately accounted for as

$$\delta p = (p - p_{\infty}) \left(\frac{1.85}{r_0}\right)^{1/2} \tag{14}$$

where 1.85 m is the booster radius and the one-half power corresponds to cylindrical spreading.

The final near-field pressure signatures obtained through the CFD methods are shown in Fig. 7. Several similarities and differences can be found between these results and those presented using F-function methods in Fig. 4. For example, the pressures here are substantially smaller than those in Fig. 4, and the rarefactions are not of comparable amplitude to the compressions, as is the case in Fig. 4. However, both the CFD and F-function methods agree that the initial bow shock is followed by a rarefaction wave associated with the airflow turning around the blunt lower portion of the geometry. Such negative pressures following the positive pressures induced by blunt bodies have been observed previously [25], as well as for cases where the tip is pointed but still has a corner or rounded region afterwards [25, 26]. As shown in Fig. 7, this rarefaction wave tends to migrate rearward at farther propagation distances. In the Falcon 9 case, it merges with a forward-migrating shock produced by the grid fins. In the following sections, nonlinear propagation modeling is employed to determine how these near-field signatures evolve during propagation to the far field.

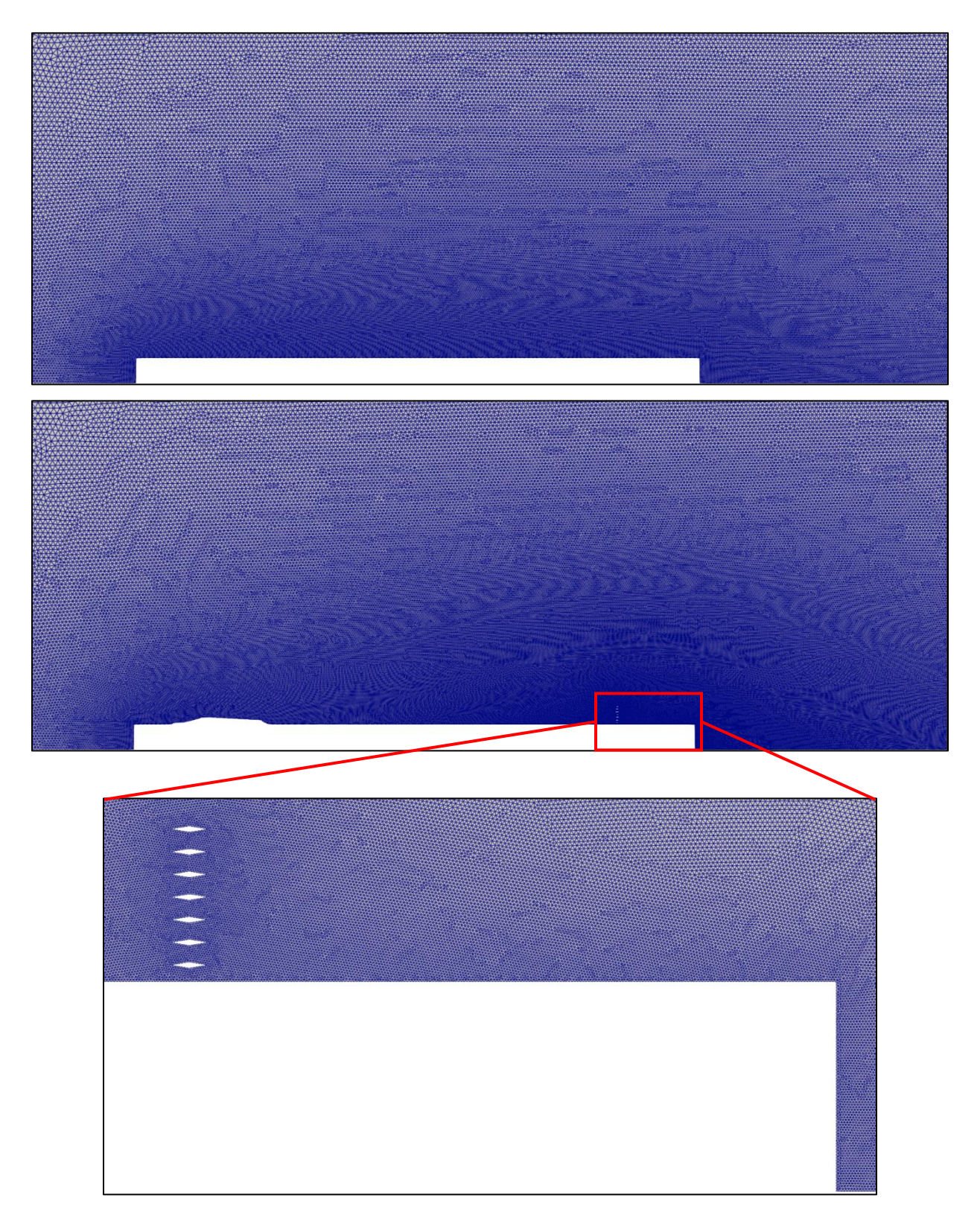


Fig. 5 Portions of the meshes used throughout the CFD simulations. (Top) the mesh for the Cylinder cases. (Middle) the mesh for the Falcon 9 cases. (Bottom), a closer view of the top of the Falcon 9 mesh, including the grid fins modeled using narrow diamonds.

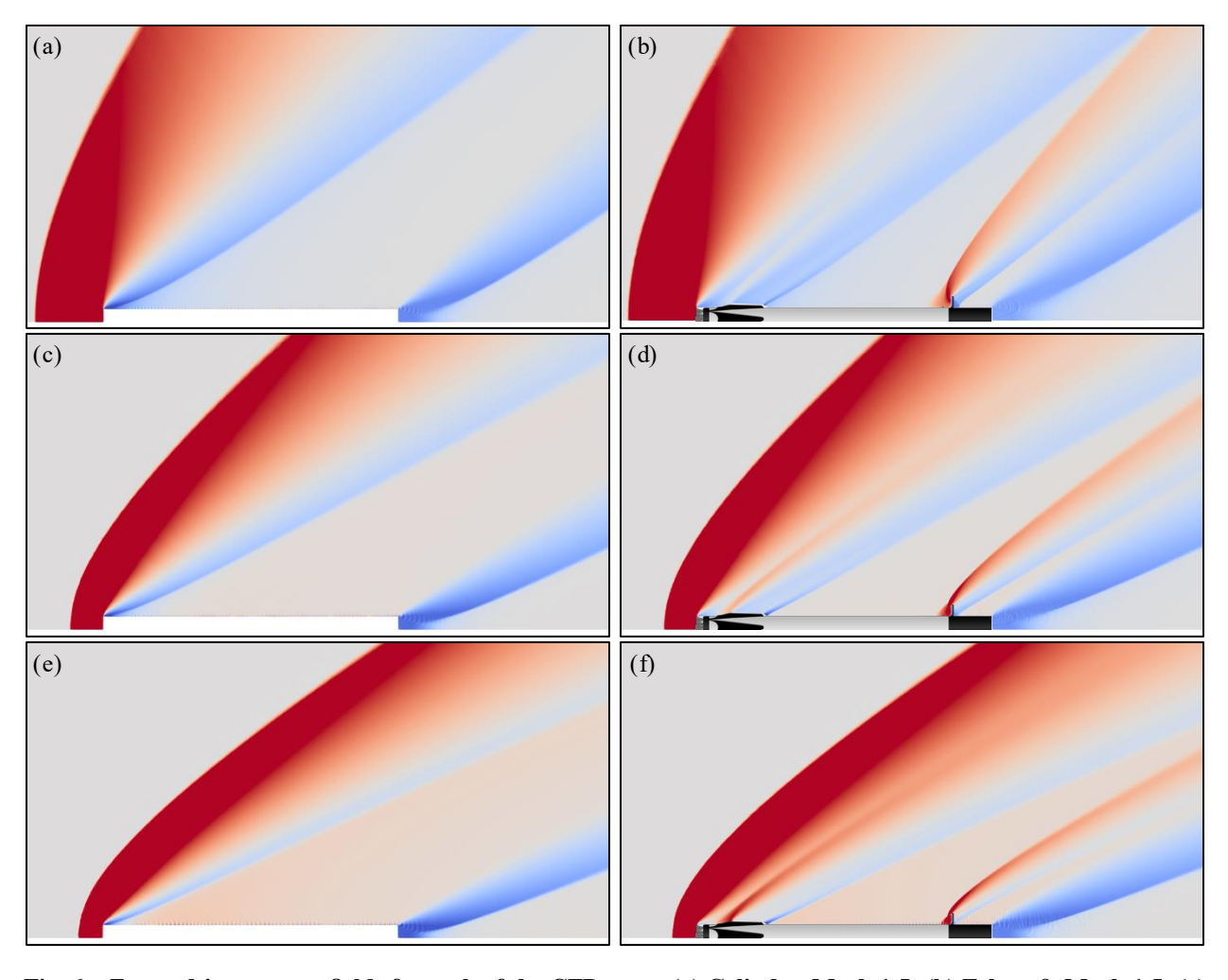


Fig. 6 Zoomed-in pressure fields for each of the CFD runs. (a) Cylinder, Mach 1.5. (b) Falcon 9, Mach 1.5. (c) Cylinder, Mach 2.0. (d) Falcon 9, Mach 2.0. (e) Cylinder, Mach 2.5. (f) Falcon 9, Mach 2.5. For the Falcon-9 simulations, a model has been superimposed on the results to aid with visualization. The color ranges are from 20 kPa (blue) to 180 kPa (red), with 100 kPa being the freestream pressure.

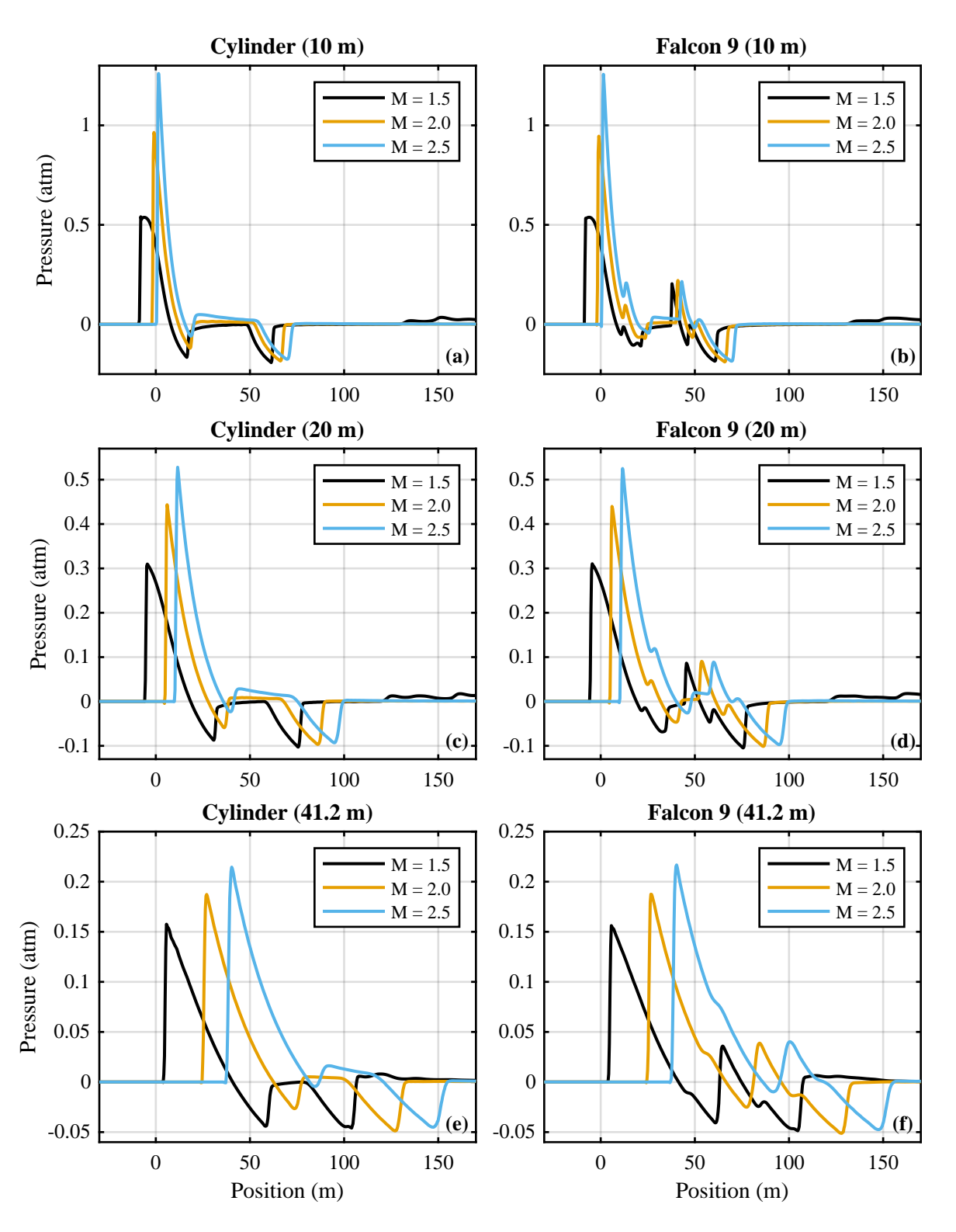


Fig. 7 The estimated near-field pressure signatures from the CFD simulations across Mach numbers and at three different distances from the geometries. Some extra pressure disturbances after the signatures are visible for the M = 1.5 cases. These were caused by minor reflections off the top boundary.

## III. Propagation Modeling

The Generalized Burgers Equation (GBE) [27, 28] models the effects of nonlinear distortion and can be expressed in lossless form for cylindrically-spreading waves as

$$\frac{\partial p}{\partial r} = \frac{\beta}{2\rho_0 c_0^3} \frac{\partial p^2}{\partial \tau} - \frac{1}{2r} p. \tag{15}$$

Here, p is the pressure disturbance, r is the propagation distance,  $\beta$  is the coefficient of nonlinearity taken to be 1.201 in air,  $\rho_0$  is the ambient density,  $c_0$  is the ambient sound speed, and  $\tau$  is the retarded time. The GBE is commonly used to study sonic boom propagation in modern software packages like PCBoom [28]. In this paper, this equation is solved numerically as follows:

1) The shock formation distance is solved for via [27]

$$r_{\text{shock}} = \frac{\rho_0 c_0^3}{\beta \frac{dp}{d\tau}|_{\text{max}}} \tag{16}$$

2) The step length is determined by

$$\Delta r = \eta r_{\text{shock}} \tag{17}$$

where  $0 < \eta < 1$  is the step size parameter.

3) The waveform distortion is calculated via the Earnshaw solution [27],

$$\tau_{\text{distort}} = \tau - \frac{\beta \Delta r}{\rho_0 c_0^3} p \tag{18}$$

- 4) The waveform is resampled back onto the original time array. This step provides numerical damping, which prevents the formation of discontinuities or triple-values waveforms.
- 5) The geometric spreading is accounted for by

$$p = \left(\frac{r_{i-1}}{r_i}\right)^{1/2} p \tag{19}$$

6) The process is repeated until the final propagation distance is reached.

To convert the pressure signatures from distance units to time units, the distance units are divided by the assumed ambient sounds speed of 343 m/s and the waveforms are resampled to 20 kHz. Additionally, the time units are then divided by the freestream Mach number  $M_{\infty}$ , which models the fact that in the far field the waves propagate normal to the shock fronts and not parallel to the source geometry.

## **IV. Results**

The near-field pressures obtained in Sec. II were propagated using the nonlinear propagation algorithm detailed in Sec. III. The results using the F-function approach are shown in Fig. 8. The near-field pressures were calculated at three different Mach numbers (1.5, 2.0, and 2.5) and propagated to four different distances (0.5, 4.0, 10, and 30 km), enabling a comparison across a range of initial conditions and propagation lengths. Across all considered conditions, the F-function approach predicts that the Falcon 9 geometry will produce a triple sonic boom. There is a trend for the central shock to be located closer to the first shock as Mach number increases. Meanwhile, the Cylinder geometry is predicted to produce a triple sonic boom at closer distances and lower Mach numbers. For farther distances and higher Mach numbers, the Cylinder predictions tend toward N-waves.

The results from propagating the CFD near-field signatures are shown in Fig. 9 using the same format as Fig. 8. The input pressure signatures were the ones at 41.2 m in Fig. 7. According to the CFD results, both the Cylinder and Falcon-9 geometries are expected to produce a triple sonic boom at all distances and across all three Mach numbers. As a general trend, the Falcon-9 geometry produces a central shock that occurs shortly before the central shock predicted for the Cylinder. This is due to the forward-migrating shock originating from the grid fins merging with the rearward-migrating

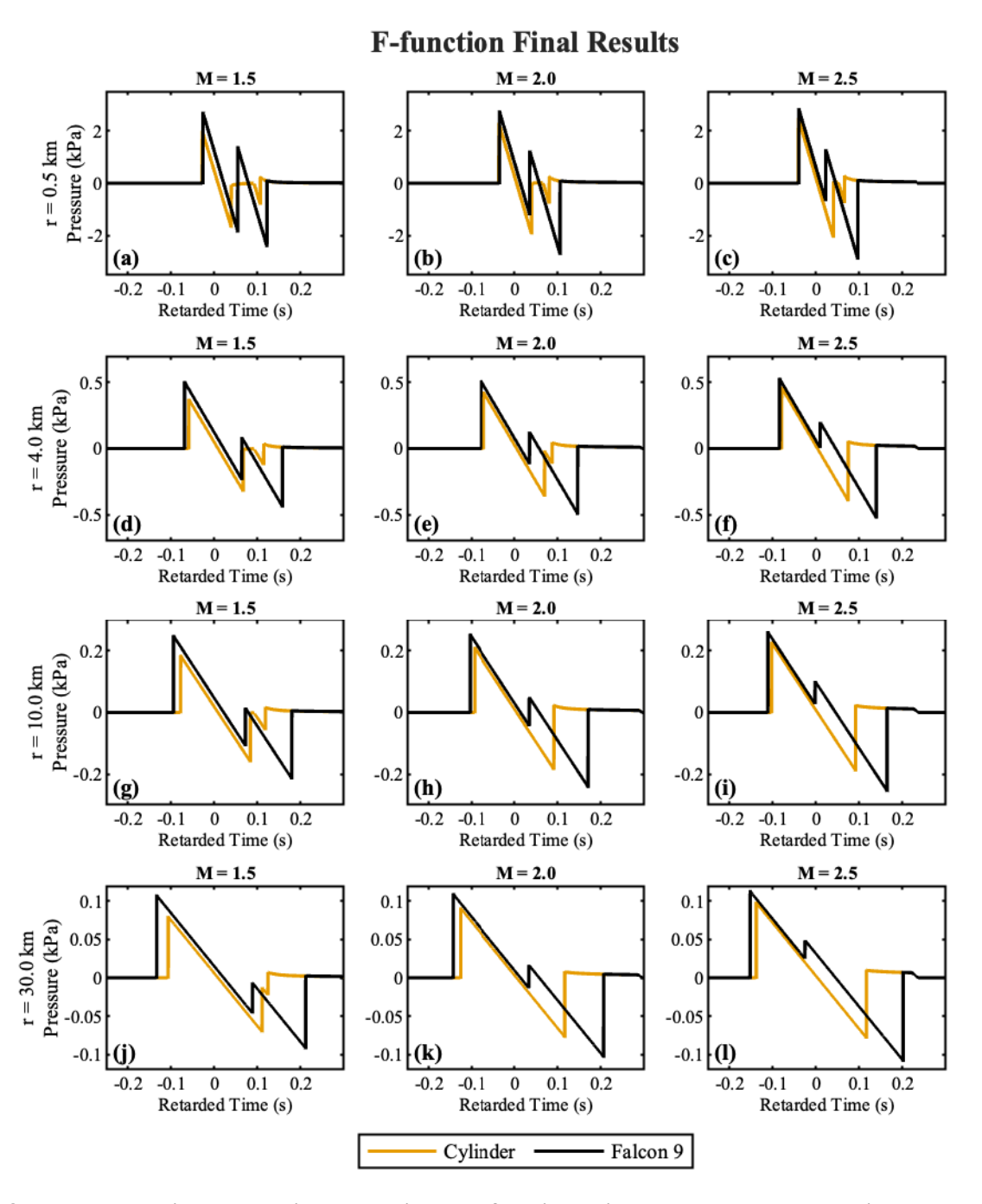


Fig. 8 Propagated signatures using the Whitham F-function as input. The Mach number is constant within columns and distance increases between rows.

rarefaction wave produced near the base of the geometry. This merging tends to slow down the overall migration of the central shock to either the front or the back of the waveform.

To increase confidence that the CFD results are physically meaningful, Fig. 10 compares a CFD prediction (M = 1.5, r = 10 km) with three representative measured signatures at 8 km away from the landing pad for three different missions. Although the central shock's amplitude is smaller in the simulated results than the measured results, its relative position within the waveform agrees well. Additionally, in both the simulated and measured waveforms, there is a small shock occurring shortly before the larger third shock. According to the CFD results, this small shock is produced by a

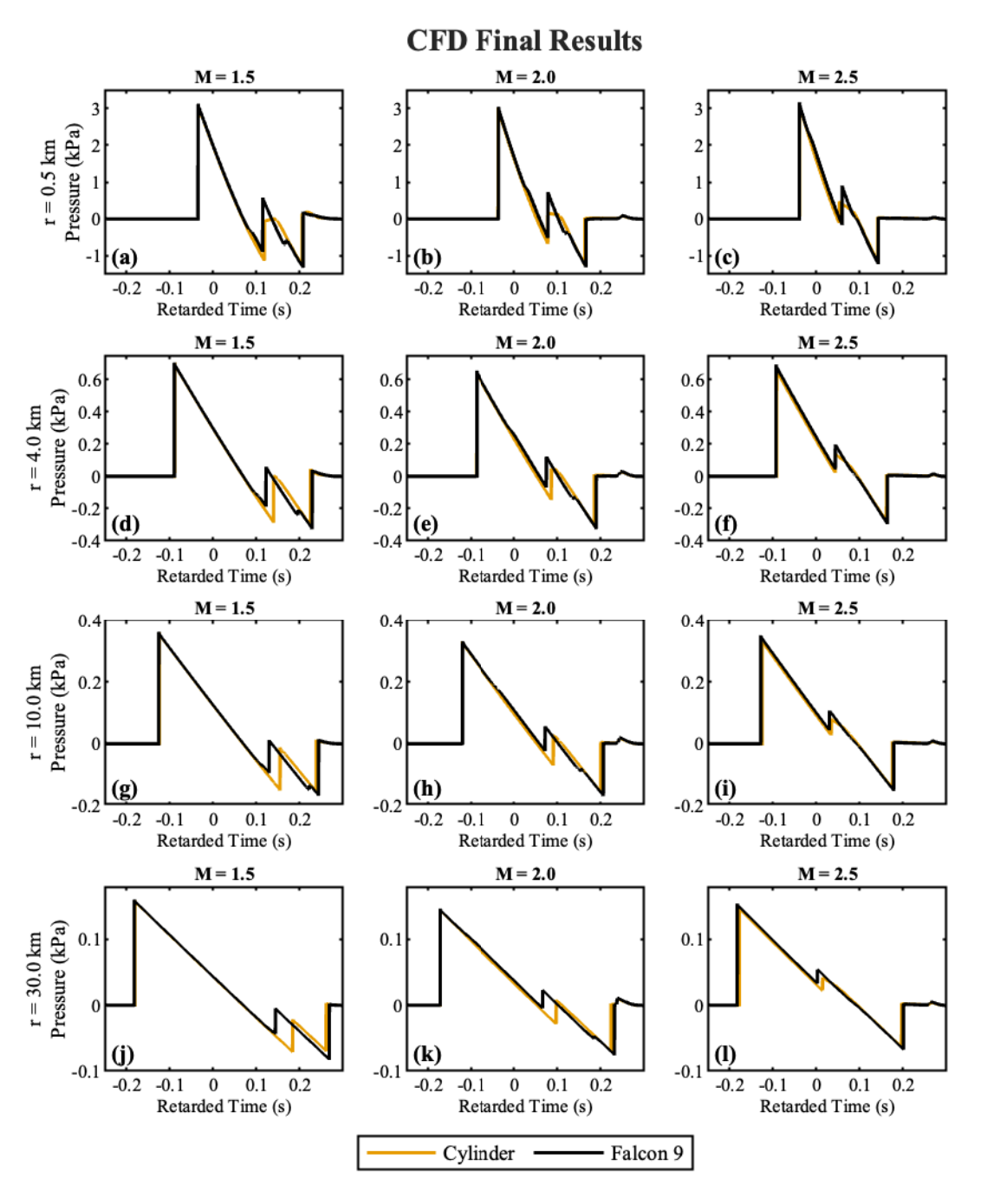


Fig. 9 Propagated signatures using the CFD results at  $r_0 = 41.2$  m from the booster as input.

rarefaction wave formed after the air flows through the grid fins and is observable in Fig. 6. This same feature is also seen in the laminar CFD simulations in Ref. [6] and was discussed as possibly originating from the grid fins by Durrant et al. [10]. Thus, it is concluded that the origin of this small shock is the rarefaction wave produced after the air flows through the grid fins. The forward-migrating shock wave produced just ahead of the grid fins merges into the central shock (increasing the central shock's amplitude some amount) while the rarefaction wave produced just behind the grid fins fails to merge with the rear shock by 8-10 km of propagation. Thus, it is concluded that the grid fins produce a forward-migrating shock wave that contributes to the far-field central shock and a rarefaction wave that can form a small minor shock before the rear shock in the final signature.

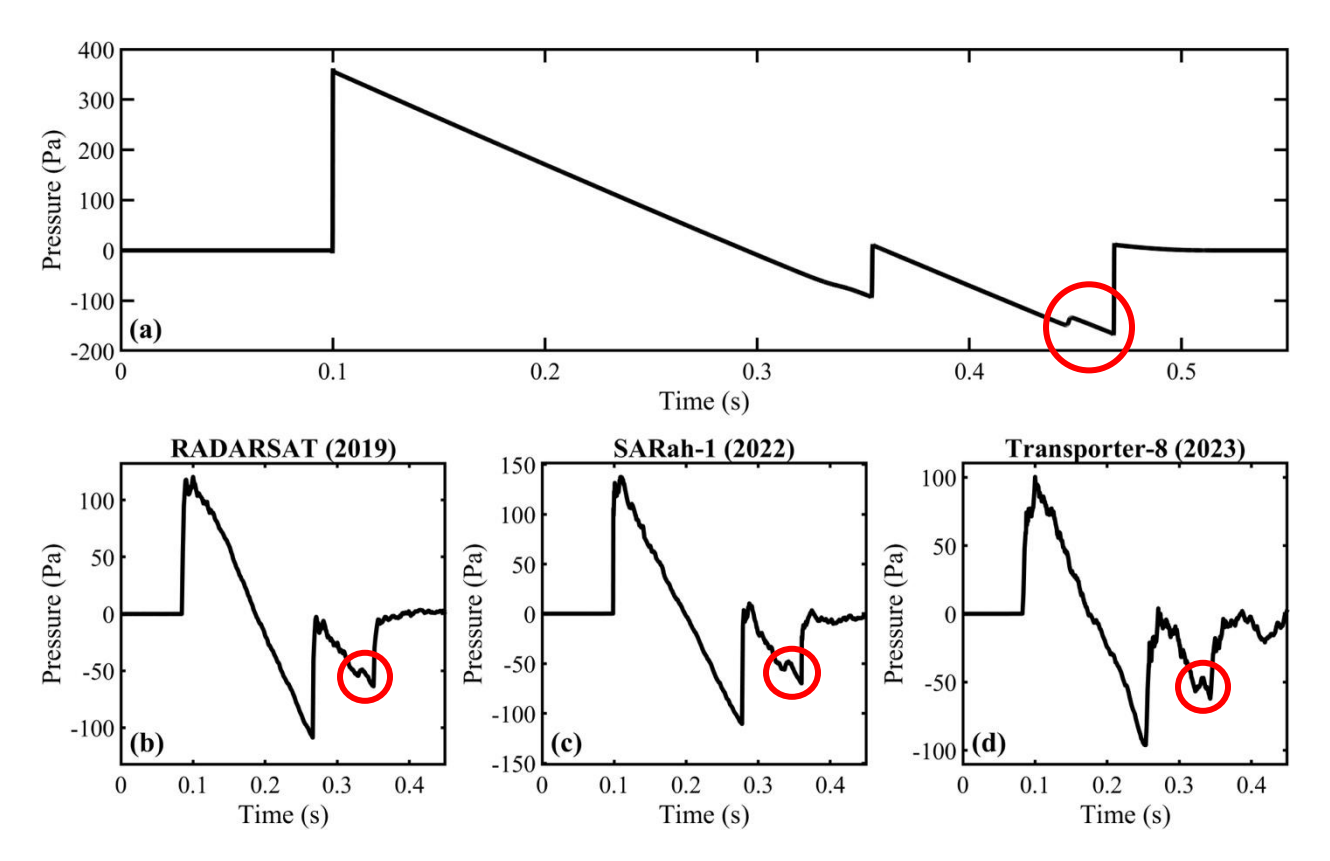


Fig. 10 Comparison between the CFD results and measurements around 10 km.

It is also important to note the discrepancy in pressure amplitude between the simulated and measured results. The measured signatures (Fig. 10(b-d)) were subject to pressure doubling due to the measurements being made on the ground, while the simulated signature (Fig. 10(a)) is free field. Were the simulated waveform to be measured on the ground (and thus experience pressure doubling) the pressures would be about seven times as great as those actually measured. Thus, although the overall waveform shapes appear to be accurate, the pressures are not.

While it is clear that the grid fins produce a compression wave and the lower parts of the booster produce a rarefaction wave, it is not clear which dominates the formation of the central shock or if they both contribute equally. The reason this is not clear is that the F-function and CFD methods, which both have pros and cons as discussed in Sec. II, disagree on the relative importance of these two features. The F-function method indicates that the grid fins are required to produce the triple boom. However, the CFD method suggests that while the grid fins play a role in determining the final central shock location and amplitude, they may not be required for producing a triple boom. The true physical answer likely lies somewhere between the results from the F-function and CFD methods.

## V. Conclusion

While most sonic booms tend toward N-waves with two shocks, flyback sonic booms from Falcon 9 rocket boosters have a triple sonic boom signature. Measured data [5] show that these triple sonic booms persist out to at least 25 km. These triple sonic booms are not fully modeled in current environmental assessments, where N-wave methods are used to predict sonic boom levels [5, 12]. Previous work [6] describes the extra, central, shock as being a combination of a rarefaction wave from the base of the vehicle and a shock wave from the grid fins. The purpose of the analyses in the present paper are to expand on the work of Ref. [6] and include a broader range of conditions and propagation distances.

In this paper, near-field source functions are generated via the Whitham F-function [16] and computational fluid dynamics (CFD). These near-field signatures are then propagated via the nonlinear generalized Burgers equation (GBE) out to distances as far as 30 km. The GBE propagation code was validated against an analytical solution for an N-wave and showed agreement within 2% for peak overpressure and shock location (see Appendix B).

Two approximate geometrical models for the Falcon-9 booster were used throughout the analyses. The lower-fidelity

model represents the booster as a simple "Cylinder". The higher-fidelity model, referred to as the "Falcon 9", included protrusions for the folded landing legs and grid fins. In the F-function method, the grid fins were also modeled as a small protrusion that allowed air to flow past while still producing a shock. In the CFD method, the grid fins were modeled as several thin diamond airfoils roughly approximating the number of struts used by the physical grid fins. This allows a more realistic approximation to the flow behavior through the grid fins.

Both the F-function and CFD methods, after propagation, predict that the Falcon-9 booster should produce a triple sonic boom. The lower portions of the geometry (i.e., the base of the rocket and the folded landing legs) produce a rarefaction wave that tends to migrate backward in the waveform during propagation. The grid fins produce a forward-migrating shock wave. These two features merge toward the middle of the waveform and account for the central shock. This agrees with the conclusion in Ref. [6].

However, the results become more complicated for the Cylinder. The F-function method predicts that the rarefaction produced by the base of the geometry is sufficiently strong to migrate backward and fully merge with the tail shock. On the other hand, the CFD results predict that this same rarefaction wave has a lower amplitude and is not sufficiently strong to migrate fully toward the rear of the waveform and merge with the tail shock. Thus the CFD near-field signature, after propagation via the GBE, predicts a triple sonic boom for both the Cylinder and Falcon-9 geometries.

The final conclusions of this paper can be summarized as follows. The first shock in the triple-boom signature is the bow shock expected at the front of all supersonic bodies. The second shock is a combination of a rearward-migrating rarefaction wave produced at the base of the geometry and a forward-migrating shock wave produced by the grid fins. The relative importance of the rarefaction wave and the shock wave is an open question because their strengths vary between the F-function and two-dimensional CFD results. The final shock is the tail or "wake" shock produced at the top of the geometry. Additionally, a minor shock often appears shortly before the final shock in measured data. This shock is successfully modeled in the CFD results as being produced by a rarefaction occurring after the flow passes through the grid fins.

While these results validate several findings in Ref. [6], there remains much work to be done in the emerging field of flyback sonic booms from reusable rockets. The current results suggest that a triple sonic boom could be produced even without grid fins, something that could be validated by studying sonic booms produced by rocket boosters with less obtrusive fin designs (e.g., Blue Origin's New Glenn rocket and RocketLab's Neutron rocket). If a deep enough understanding of the physics behind these rocket flyback sonic booms is developed, then perhaps design changes could be incorporated to optimize the boom shape. Additionally, all this research has assumed the vehicle axis is perfectly aligned with the freestream, while actual rocket boosters tend to be angled somewhat relative the to the freestream. Thus, the effects of breaking the axisymmetry assumption need to be studied, including effects of lift. Finally, the effects of having three primary shocks vs an N-wave have not yet been studied on structures, wildlife, or communities.

#### Acknowledgments

A portion of this work was funded by the US Air Force/Space Force and supported by USACE.

A portion of this work was also funded by an appointment to the Department of Defense (DOD) Research Participation Program administered by the Oak Ridge Institute for Science and Education (ORISE) through an interagency agreement between the U.S. Department of Energy (DOE) and the DOD. ORISE is managed by ORAU under DOE contract number DE-SC0014664. All opinions expressed in this paper are the author's and do not necessarily reflect the policies and views of DOD, DOE, or ORAU/ORISE.

## **Appendix A: Further CFD Results**

The zoomed-in CFD results shown in Section II enable a better view of the flow near the vehicle. It is also useful to see the flow throughout the entire domain. This can help validate the propagation results from a qualitative perspective, as the shock coalescence can also be observed in the computational domain for the CFD calculations. The full-domain results for the Cylinder are shown in Fig. 11 and the same results for the Falcon 9 are shown in Fig. 12. In all cases, the top boundary failed to perfectly transmit waves, and so partial reflections are visible. In some cases throughout this paper, especially at lower Mach numbers, these reflections are visible in the signatures (e.g., Figs. 7 at Mach 1.5 and 9(b)). Of course, these minor pressure disturbances after the sonic boom are not physical.

In Section IV, only the pressures along the line parallel to and 41.2 m from the geometries were used for propagation. For completeness, Fig. 13 shows the results for propagating the Falcon-9 near-field pressures at 10, 20, and 41.2 m to the same four propagation distances shown in Section IV. Although there is some dependence on which initial distance is

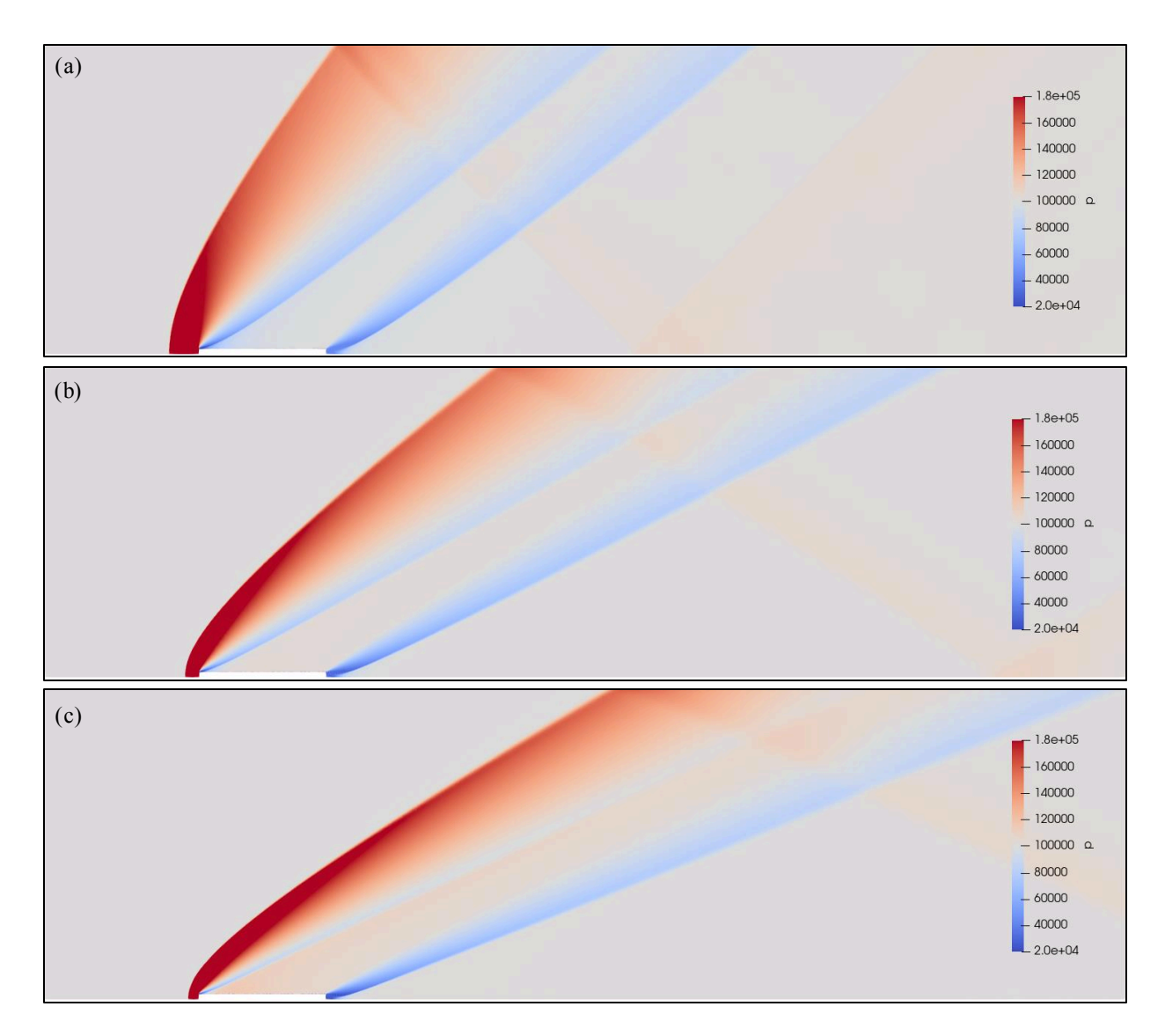


Fig. 11 CFD results for the Cylinder over the full computational domain at (a) Mach 1.5, (b) Mach 2.0, and (c) Mach 2.5.

chosen, the results remain qualitatively the same, without any change to the final conclusions in this paper. Although not shown, the results using the Cylinder simulations are also qualitatively the same when using different input distances.

It is important to also note that the propagation model assumes "weak" shocks, in which the pressure excursions are an order of magnitude less than ambient pressure [27]. Extracting the signature farther from the geometry tends to better meet this assumption, with the caveat that the simulations are two-dimensional and shock coalescence in two dimensions will occur faster than in a three-dimensional case. Strong shock extrapolation methods like those used in Refs. [29, 30] could be employed in the future to further improve the final signatures.

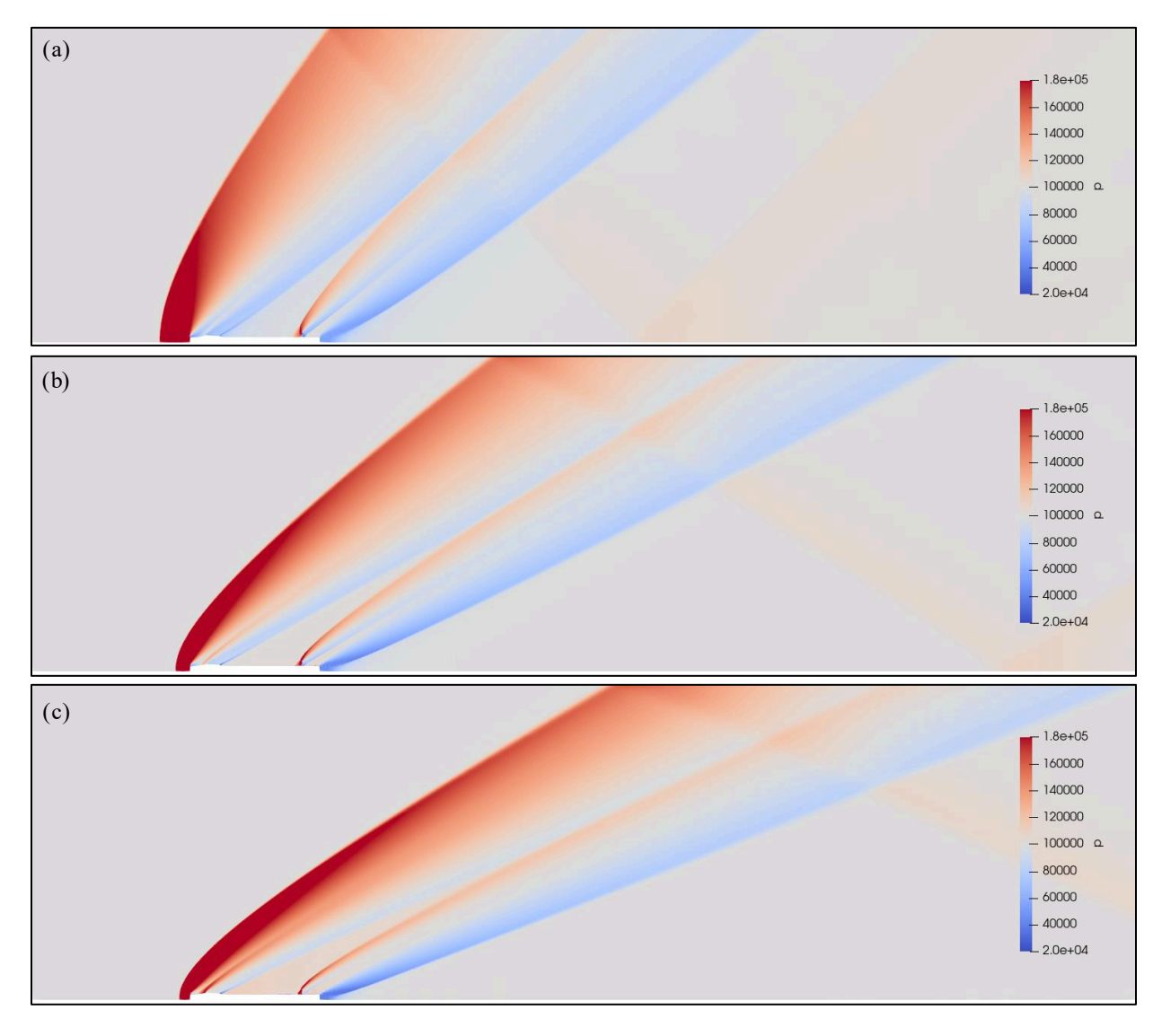


Fig. 12 CFD results for the Falcon 9 over the full computational domain at (a) Mach 1.5, (b) Mach 2.0, and (c) Mach 2.5.

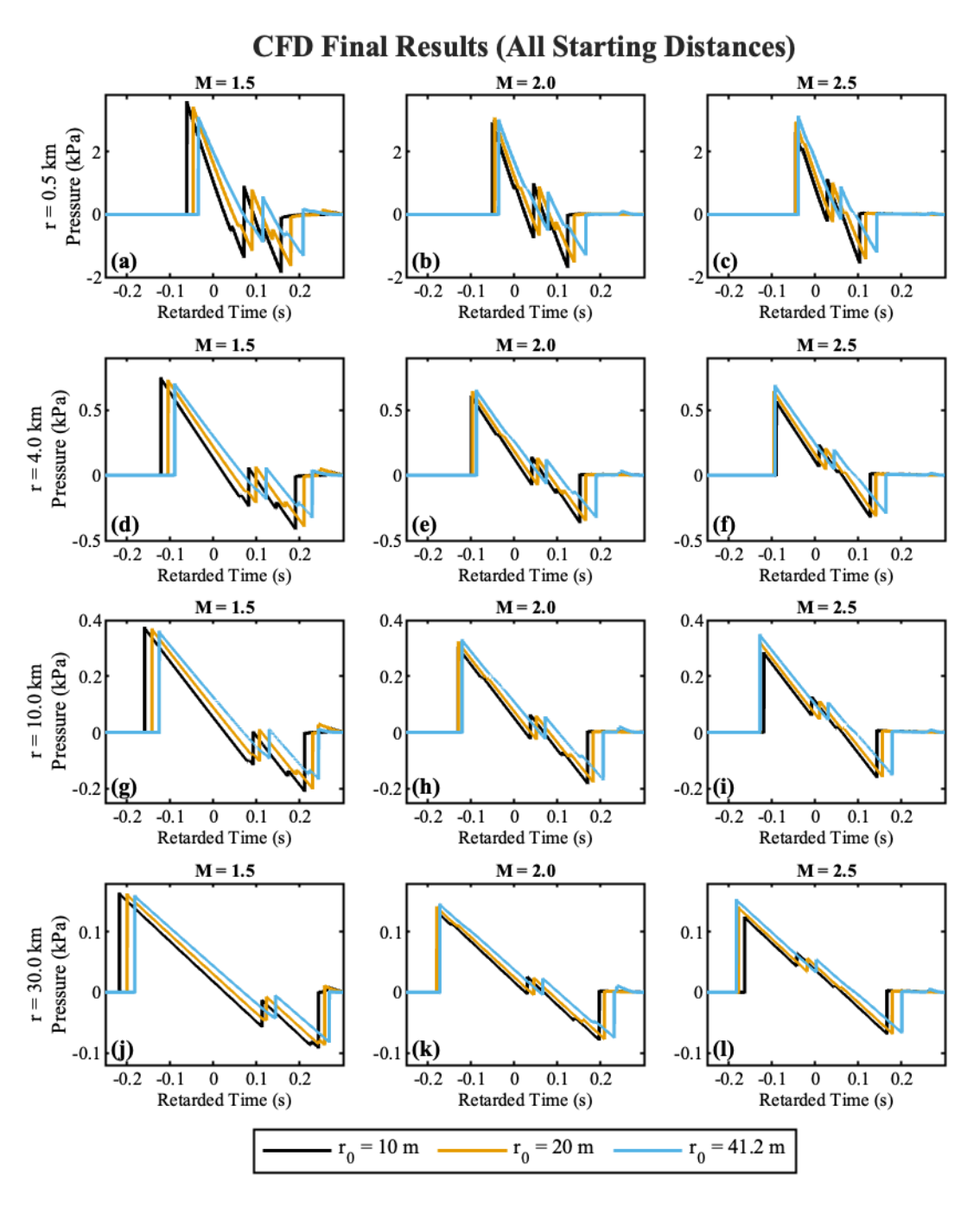


Fig. 13 Comparing the propagated signatures for the Falcon 9 using three different distances for the near-field pressures. This is to roughly assess the uncertainty in the final results due to the choice of near-field distance.

# **Appendix B: Propagation Code Validation**

It is important to validate that the propagation code works properly. The test case shown in this paper is a comparison with an analytical solution for a planar N-wave [27]. For an N-wave with an initial overpressure  $p_0$  and initial duration  $2T_0$  between the front and tail shocks, the pressure decays as

$$p(r) = \frac{p_0}{\sqrt{1 + \frac{\beta p_0}{\rho_0 c_0^3 T_0}} r}$$
 (20)

and the location of the front shock changes as

$$T(r) = T_0 \sqrt{1 + \frac{\beta p_0}{\rho_0 c_0^3 T_0}} r. \tag{21}$$

Figure 14 shows the results of testing the propagation code against the analytic solution for an N-wave with  $p_0 = 10$  kPa and  $T_0 = 0.2$  s. Subplot (a) shows the input waveform (grey) and the final waveform after propagation with the code (orange) alongside the analytical solution in black. The front shock peak overpressure is considered alongside the analytical result in subplot (b), with the percent error shown in (c). The location of the front shock is shown in subplot (d), with the percent error shown in (e). Overall, the peak pressure error is within 2% and the shock location error is within 1% out to 30 km of plane-wave propagation. Similarly-accurate results were found when using an analytic solution for the peak overpressure of a cylindrically-spreading N-wave [27].

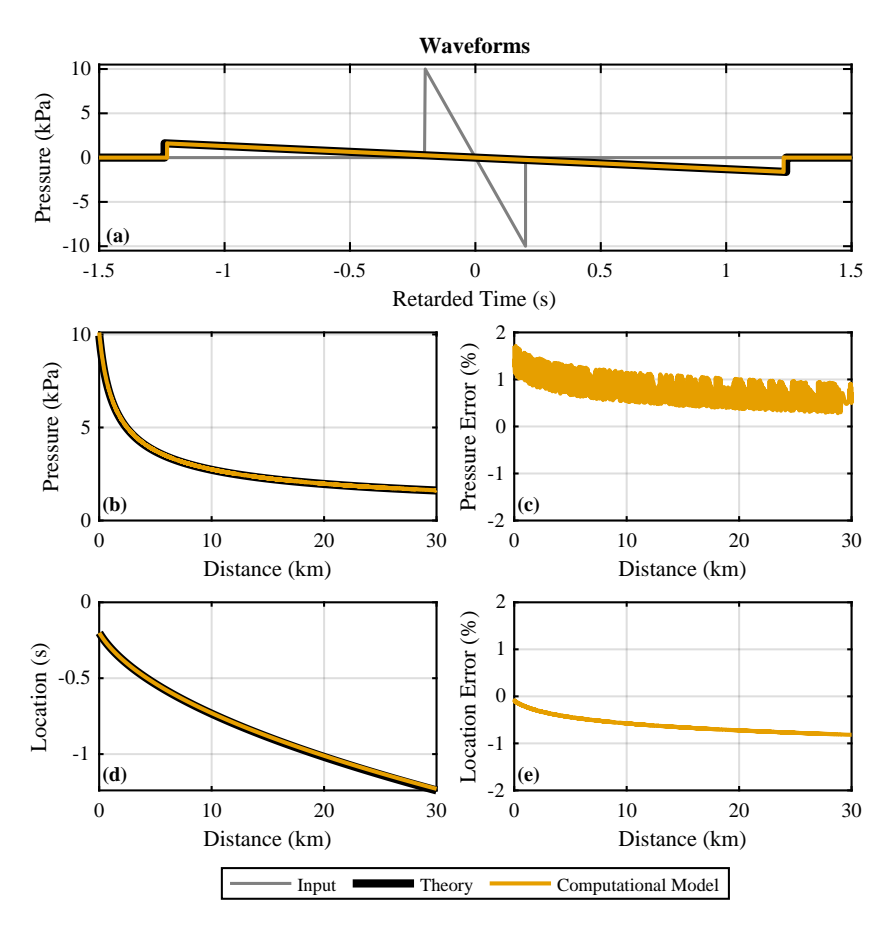


Fig. 14 Propagation of an N-wave through the Burgers equation code and comparison to analytical results for 30 km of plane-wave propagation. (a) the input and final waveforms. (b) the front shock overpressure compared to analytical results. (c) the percent error for the front shock overpressure. (d) the front shock location compared to analytical results. (e) the percent error for the front shock location.

#### References

- [1] Hilton, D. A., Henderson, H. R., and McKinney, R., "Sonic-boom ground-pressure measurements from Apollo 15," Report, 1972. URL https://ntrs.nasa.gov/citations/19720023246, NASA TN D-6950.
- [2] Henderson, H. R., and Hilton, D. A., "Sonic-boom ground pressure measurements from the launch and reentry of Apollo 16," Report, 1974. URL https://ntrs.nasa.gov/citations/19740023384, NASA TN D-7606.
- [3] Henderson, H. R., and Hilton, D. A., "Sonic-boom measurements in the focus region during the ascent of Apollo 17," Report, 1974. URL https://ntrs.nasa.gov/citations/19750005520, NASA TN D-7806.
- [4] Maglieri, D. J., Henderson, H. R., Massey, S. J., and Stansbery, E. G., "A Compilation of Space Shuttle Sonic Boom Measurements," Report, 2011. URL https://ntrs.nasa.gov/citations/20110011322, NASA/CR-2011-217080.
- [5] Anderson, M. C., Gee, K. L., and Nyborg, K., "Flyback sonic booms from Falcon-9 rockets: Measured data and some considerations for future models," *Proc. Mtgs. Acoust.*, Vol. 54, No. 1, 2024, p. 040005. https://doi.org/10.1121/2.0001916.
- [6] Anderson, M. C., and Gee, K. L., "Why does the Falcon-9 booster make a triple sonic boom during flyback? An initial analysis," *JASA Express Letters*, Vol. 5, No. 2, 2025, p. 023601. https://doi.org/10.1121/10.0035649.
- [7] SpaceX, "Falcon 9: First Orbital Class Rocket Capable of Reflight,", 2024. URL www.spacex.com/vehicles/falcon-9/, last viewed: 05-29-2025.
- [8] SpaceX, "Transporter-8 Mission,", 2023. URL www.youtube.com/watch?v=zO3luySkHQU&t=853s, last viewed: 05-29-2025.
- [9] Maglieri, D. J., Bobbitt, P. J., Plotkin, K. J., Shepherd, K. P., Coen, P. G., and Richwine, D. M., "Sonic Boom: Six Decades of Research," Report, NASA Langley Research Center, 2014. URL https://ntrs.nasa.gov/citations/20150006843, NASA-SP-2014-622.
- [10] Durrant, J. T., Anderson, M. C., Gee, K. L., Mathews, L. T., and Hart, G. W., "Initial comparison of a Falcon-9 reentry sonic boom with other launch-related noise," Proc. Mtgs. Acoust., 2022. https://doi.org/10.1121/2.0001579.
- [11] Durrant, J. T., Anderson, M. C., Bassett, M. S., Gee, K. L., Hart, G. W., Batelaan, R. H., Lawrence, D. C., and Hall, L. K., "Overview and spectral analysis of the Falcon-9 SARah-1 launch and reentry sonic boom," Proc. Mtgs. Acoust., 2023. https://doi.org/10.1121/2.0001767.
- [12] Anderson, M. C., and Gee, K. L., "Sonic Boom Measurements From the SpaceX Transporter-8 Falcon-9 Rocket Landing at Vandenberg Space Force Base," 30th AIAA/CEAS Aeroacoustics Conference, AIAA 2024-3188, 2024. https://doi.org/10.2514/ 6.2024-3188, see also: https://doi.org/10.2514/6.2024-3188.c1.
- [13] Gee, K. L., Pulsipher, N. L., Kellison, M. S., Mathews, L. T., Anderson, M. C., and Hart, G. W., "Starship super heavy acoustics: Far-field noise measurements during launch and the first-ever booster catch," *JASA Express Letters*, Vol. 4, No. 11, 2024, p. 113601. https://doi.org/10.1121/10.0034453.
- [14] Charbonnier, D., Vos, J., Marwege, A., and Hantz, C., "Computational fluid dynamics investigations of aerodynamic control surfaces of a vertical landing configuration," CEAS Space Journal, Vol. 14, No. 3, 2022, pp. 517–532. https://doi.org/10.1007/s12567-022-00431-6.
- [15] Stanley Creative, "Falcon 9 SpaceX,", 2023. URL https://sketchfab.com/3d-models/falcon-9-spacex-394f7cf52d124bbd9db69f24d1ff2f08.
- [16] Whitham, G. B., "The flow pattern of a supersonic projectile," *Communications on Pure and Applied Mathematics*, Vol. V, 1952, pp. 301–348. https://doi.org/10.1002/cpa.3160050305.
- [17] Bykerk, T., Kirchheck, D., and Karl, S., "Reconstruction of Wind Tunnel Tests using CFD for a Reusable First Stage during Rocket Retro-Propulsion," 9th European Conference for Aeronautics and Space Sciences (EUCASS), 2022. https://doi.org/10.13009/EUCASS2022-4494.
- [18] Marwege, A., Riemer, J., Klevanski, J., Gülhan, A., Ecker, T., Reimann, B., and Dumont, E., "First Wind Tunnel Data of CALLISTO - Reusable VTVL Launcher First Stage Demonstrator," EUCASS 2019, 2019. https://doi.org/10.13009/ EUCASS2019-350.
- [19] Carlson, H. W., and Mack, R. J., "A Study of the Sonic-Boom Characteristics of a Blunt Body at a Mach Number of 4.14," NASA Technical Paper, 1977. URL https://ntrs.nasa.gov/citations/19770025128, NASA-TP-1015.

- [20] Gottlieb, J. J., and Ritzel, D. V., "Analytical Study of Sonic Boom from Supersonic Projectiles," *Prog. Aerospace Sci.*, Vol. 25, 1988, pp. 131–188. https://doi.org/10.1016/0376-0421(88)90006-1.
- [21] Geuzaine, C., and Remacle, J., "Gmsh,", 2024. URL http://gmsh.info/, last viewed: 05-29-2025.
- [22] OpenFOAM, "OpenFOAM 11,", 2024. URL https://www.openfoam.com, last viewed: 05-29-2025.
- [23] SimScale, "K-Omega Turbulence Models,", 2025. URL https://www.simscale.com/docs/simulation-setup/global-settings/k-omega-sst/, Last Viewed: 04-21-2025.
- [24] Direct, C., "Notes on Computational Fluid Dynamics: General Principles,", 2025. URL https://doc.cfd.direct/notes/cfd-general-principles/specific-dissipation-rate, Last Viewed: 04-21-2025.
- [25] Shrout, B. L., Mack, R. J., and Dollyhigh, S. M., "A wind-tunnel investigation of sonic-boom pressure distributions of bodies of revolution at Mach 2.96, 3.83, and 4.63," NASA Technical Note, 1971. URL https://ntrs.nasa.gov/citations/19710012486, NASA TN D-6195.
- [26] Carlson, H. W., Mack, R. J., and Morris, O. A., "A wind-tunnel investigation of the effect of body shape on sonic-boom pressure distributions," NASA Technical Note, 1965. URL https://ntrs.nasa.gov/citations/19660001963, NASA TN D-3106.
- [27] Hamilton, M. F., and Blackstock, D. T., Nonlinear Acoustics, Acoustical Society of America, 2008. ISBN: 0-9744067-5-9.
- [28] Lonzaga, J. B., Page, J. A., Downs, R. S., Kaye, S. R., Shumway, M. J., Loubeau, A., and Doebler, W. J., "PCBoom 7 Technical Reference," Report, 2022. URL https://ntrs.nasa.gov/citations/20220007177.
- [29] Hicks, R. M., Mendoza, J. P., and Thomas, C. L., "Pressure signatures for the Apollo command module and the Saturn 5 launch vehicle with a discussion of strong shock extrapolation procedures," NASA Technical Memorandum, 1972. URL https://ntrs.nasa.gov/citations/19730005177, NASA-TM-X-62117.
- [30] Garcia, F. J., Hicks, R. M., and Mendoza, J. P., "A wind tunnel flight correlation of Apollo 16 sonic boom," NASA Technical Memorandum, 1973. URL https://ntrs.nasa.gov/citations/19730012346, NASA-TM-X-62073.